

# Graphite and Graphene Fairy Circles: A Bottom-Up Approach for the Formation of Nanocorrals

*Thanh Hai Phan,<sup>\*,1,2,γ</sup> Hans Van Gorp,<sup>1,γ</sup> Zhi Li,<sup>1</sup> Thi Mien Trung Huynh,<sup>1,3</sup> Yasuhiko Fujita,<sup>1</sup> Lander Verstraete,<sup>1</sup> Samuel Eyley,<sup>4</sup> Wim Thielemans,<sup>4</sup> Hiroshi Uji-i,<sup>1</sup> Brandon E. Hirsch,<sup>1</sup> Stijn F. L. Mertens,<sup>1,5</sup> John Greenwood,<sup>1</sup> Oleksandr Ivasenko,<sup>\*,1</sup> Steven De Feyter<sup>\*,1</sup>*

<sup>1</sup>KU Leuven, Department of Chemistry, Division of Molecular Imaging and Photonics, Leuven, Celestijnenlaan 200F, B-3001, Leuven, Belgium

<sup>2</sup>Quy Nhon University, Department of Physics, 170 An Duong Vuong, Quy Nhon, Vietnam

<sup>3</sup>Quy Nhon University, Department of Chemistry, 170 An Duong Vuong, Quy Nhon, Vietnam

<sup>4</sup> KU Leuven, Department of Chemical Engineering, Renewable Materials and Nanotechnology Group, Campus Kortrijk, Etienne Sabbelaan 53, 8500 Kortrijk, Belgium

<sup>5</sup> Lancaster University, Department of Chemistry, Lancaster LA1 4YB, United Kingdom

Corresponding authors: [phanthanhhai@qnu.edu.vn](mailto:phanthanhhai@qnu.edu.vn); [oleksandr.ivasenko@kuleuven.be](mailto:oleksandr.ivasenko@kuleuven.be); [steven.defeyter@kuleuven.be](mailto:steven.defeyter@kuleuven.be)

<sup>γ</sup> These authors contributed equally to this work

**ABSTRACT:** A convenient covalent functionalization approach and nanopatterning method of graphite and graphene is developed. In contrast to expectations, electrochemically activated dediazotization of a mixture of two aryl diazonium compounds in aqueous media leads to a spatially inhomogeneous functionalization of graphitic surfaces, creating covalently modified surfaces with quasi-uniform spaced islands of pristine graphite or graphene, coined nanocorrals. Cyclic voltammetry (CV) and chronoamperometry (CA) approaches are compared. The average diameter (45–130 nm) and surface density (20 to 125 corrals/ $\mu\text{m}^2$ ) of these nanocorrals are tunable. These chemically modified nanostructured graphitic (CMNG) surfaces are characterized by atomic force microscopy, scanning tunneling microscopy, Raman spectroscopy and microscopy, and x-ray photoelectron spectroscopy. Mechanisms leading to the formation of these CMNG surfaces are discussed. The potential of these

surfaces to investigate supramolecular self-assembly and on-surface reactions under nanoconfinement conditions is demonstrated.

**Keywords:** covalent functionalization, electrochemical grafting, cyclic voltammetry, chronoamperometry, nano-confined self-assembly, on-surface polymerization

Nanopatterning surfaces is important in view of applications in nanoscience and nanotechnology. Various approaches have been developed, targeting different length scales, functionalities, and substrates.<sup>1-5</sup> Those processes can be divided in top-down and bottom-up approaches or combinations thereof and they have been shown to be extremely versatile.<sup>6-10</sup> Among approaches that nanostructure surfaces, those based on molecule-based functionalization take a special place.<sup>11-15</sup> Decorating surfaces with molecules and (bio)polymers in a nanostructured way leads to an almost unlimited variation of the local properties at the nanoscale.

Graphene and graphite are carbon based surfaces that are receiving a lot of attention because of their relevance in materials sciences.<sup>16-18</sup> Multiple molecule based functionalization protocols have been developed.<sup>19-29</sup> Among those that result in nanopatterning, supramolecular self-assembly plays a prominent role, as it often leads to two-dimensional (poly)crystalline films.<sup>21-23,30</sup> However, the non-covalent nature of the molecule-substrate interactions provides the layers with only limited stability.

An alternative molecule-based functionalization approach of graphitic substrates is their covalent modification. Several chemistries have been developed, diazonium chemistry being the most popular one, to functionalize graphene and graphite covalently, in a process called grafting.<sup>19,24,29,31,32</sup> Once covalently linked *via* a hit-and-stick mechanism, the molecules are immobilized, resulting in a non-periodic homogeneous functionalization. This method can be combined with flow chemistry, giving rise to a *local* covalent functionalization,<sup>33</sup> or nanolithography methods, leading to *local* removal of grafted molecules.<sup>34,35</sup> Recently, we developed the latter approach using a scanning tunneling microscopy (STM) based nanoshaving technique: molecules are locally removed from the surface, with an accuracy of a few

nm, leaving behind pristine graphite or graphene.<sup>29,36,37</sup> While this lithography approach gives rise to a very good control of the shape, size and orientation of the pristine graphene or graphite islands, the nature of the approach limits upscaling possibilities.

Protocols to *nanopattern* graphitic substrates *via covalent chemistry* on a macroscopic scale, so not local, are extremely rare. Periodic covalent functionalization, rendering the graphitic surface partially and periodically pristine, was demonstrated based on the use of masks, *e.g.* self-assembled beads, that cover the surface in a periodic way.<sup>32,38</sup> This multistep approach is tedious and requires advanced practical skills. In a bottom-up strategy developed by Xia *et al.*, precursor molecules are organized on the surface *via* self-assembly prior to grafting.<sup>39</sup> In this way, linear stripes of grafted molecules were formed, their interrow distance controlled by spacer units. However, the resulting surface was still fully covered with templating molecules. Recently, Tobe *et al.* presented a concept of using removable self-assembled alkanes as masks to guide the covalent functionalization in between the alkane rows. In their approach, the spacing between the rows of grafted molecules is determined by the length of the alkane molecules.<sup>40</sup>

Here we demonstrate that some nanostructures can be conveniently formed on graphene and graphite surfaces *via* functionalization using mixtures of two aryl diazonium salts. These diazonium derivatives are reduced electrochemically to generate aryl radicals, which attack the graphite electrode to form covalent bonds with the surface. By contrast with the expected formation of a randomly grafted surface, the graphitic surfaces are nanopatterned with quasi-circular pristine graphene or graphite islands resulting from a non-homogeneous covalent functionalization mechanism. The diameter of these islands can be tuned. A potential mechanism is discussed. Furthermore, we demonstrate various applications ranging from site-selective supramolecular self-assembly to reactivity under nanoconfinement conditions.

## RESULTS AND DISCUSSION

Since pristine graphene and graphite are rather chemically inert, surface modification requires highly reactive reagents. A popular way to functionalize these surfaces is *via* radicals generated from aryl diazonium salts in order to form chemical bonds. In the electrochemical method, aryl diazonium is electrochemically reduced near an electrode surface, generating aryl radicals that attack the electrode surface in order to form covalent bonds. Due to low stability of many diazonium salts, they are often generated *in situ* from anilines. This process is called diazotization, and has been used by us and many others to prepare precursors for the functionalization of different substrates.<sup>24,29,39-41</sup> In aqueous solution, diazotization is carried out by mixing anilines with nitrous acid that is generated *ex tempore* from sodium nitrite and a mineral acid. With the intention to form homogeneously covered monocomponent and bicomponent functionalized graphitic surfaces, we exposed the graphitic substrates to supporting electrolyte containing 4-nitrobenzenediazonium (NBD), 3,5-bis-*tert*-butylbenzenediazonium (TBD) or a mixture of both (Figure 1). The choice for NBD and TBD was motivated by their well-characterized functionalization of graphite and graphene.<sup>24,29,36</sup> The NBD and TBD solutions, or their mixtures, were immediately transferred to an electrochemical cell to perform grafting. Based on the previously established cyclic voltammetry (CV) protocol,<sup>24</sup> the substrate potential was swept three times (scan rate: 50 mV/s) from +0.5 V to -0.4 V (*vs.* Ag/AgCl) and back. All functionalized samples were then rinsed with Milli-Q water, followed by hot toluene (90 °C), again Milli-Q water, and finally dried under a gentle stream of argon.

Before considering the voltammetric behavior of the mixture of diazonium salts, we compare their separate behavior, Figure 2a (blue and green traces). During the first cycle, TBD displays an exponentially increasing reduction current before reaching a peak value, followed by an overall decreasing current as mass transport in solution becomes rate-limiting. NBD, by contrast, shows two maxima that are overall much broader and less well-defined than for TBD. Importantly, the onset

potential for reduction is roughly 500 mV less negative for NBD than for TBD. This onset potential reflects the ease with which the electrochemical reduction starts and is strongly affected by the electron-withdrawing or -donating character of substituents on the arene ring<sup>42</sup>: electron-withdrawing substituents (*e.g.* the nitro group in NBD) increase the reactivity of diazonium salts towards reduction. Electron-donating substituents (*e.g.* the *tert*-butyl groups in TBD) have the opposite effect and require a more negative potential for electrochemical reduction to start.

Despite being one of the most abundantly studied diazonium salts in the context of grafting (in particular on glassy carbon), the details of NBD electroreduction are still debated.<sup>43</sup> Part of the complexity stems from the fact that the nitro group is electroactive and can be reduced to hydroxylamine (–NHOH). Furthermore, once reduction of the diazonium salt starts, radical attack of neighboring molecules in solution and of the electrode surface progressively cause chemically irreversible changes. By comparison, the steric hindrance caused by the substituents in TBD limits the variation of follow-up reactions that are possible, which we consider the main reason for an overall better-behaved cyclic voltammogram.

Successful functionalization is confirmed by Raman spectroscopy (Figure 2b) by the appearance of the characteristic D band ( $1335\text{ cm}^{-1}$ ), which is absent on pristine graphite.<sup>44</sup> The degree of functionalization is quantified by measuring the  $I_D/I_G$  ratio which is  $0.022 \pm 0.001$  for NBD and  $0.089 \pm 0.024$  for TBD. Furthermore, each bright feature in the STM topography images (Figures 2f-h) can be attributed to an individual grafting site. In line with our previous study, STM shows that the monocomponent systems cover the graphite surface in a quite homogeneous fashion. In contrast to TBD where the *tert*-butyl groups protect the molecule from further radical attack, ensuring monolayer coverage, in the case of NBD dendritic growth is possible, which was previously confirmed by atomic force microscopy (AFM) showing significantly higher topographic features.<sup>24,31,34</sup>

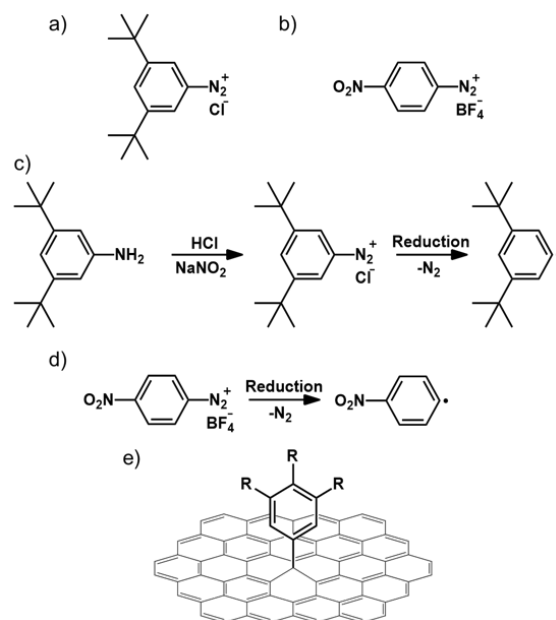


**Figure 1.** Structural formula of (a) 3,5-bis-*tert*-butylbenzenediazonium (TBD) chloride and (b) 4-nitrobenzenediazonium (NBD) tetrafluoroborate. (c) Reaction schematic of the diazotization process, starting from 3,5-bis-*tert*-butylaniline in order to *in situ* produce TBD, followed by electrochemical reduction to generate aryl radicals. (d) Reaction schematic of the reduction of NBD to a nitrophenyl radical. When these radicals are generated close to the graphitic substrate, they are able to attack the surface creating a covalent bond.

We now turn our attention to the 1:1 mixture of NBD and TBD, Figure 2a (orange trace). The overall shape of the curve, including the clear exponential increase towards the current peak, closely resembles the CV of TBD alone. The entire curve, however, is shifted towards more positive potentials by approximately 300 mV. We hypothesize that in the mixture, the presence of TBD limits the side reactions in which NBD can participate, so that the voltammetric profile approaches that of pure TBD. At the same time, the more easily reduced NBD may act as a redox mediator towards reduction of TBD at potentials where TBD alone cannot be reduced, effectively facilitating this process and yielding a voltammogram in between those of pure NBD and TBD. Finally, and anticipating the Mechanistic Considerations section later in this paper, the thermodynamics and kinetics of gas bubble nucleation and growth (N<sub>2</sub> and NO, generated during the reduction of the diazonium salt and of excess HNO<sub>2</sub>,

respectively) on the electrode surface is complex<sup>45</sup> and with certainty factors into the voltammetric behavior.

Raman spectra show again the appearance of the characteristic D peak (Figure 2b) with an intermediate  $I_D/I_G$  ratio of  $0.042 \pm 0.028$ . To our surprise, however, in contrast to the anticipated homogeneous coverage of the surface by both compounds, quasi-periodic arrays of disk-like molecule-free islands are observed by both AFM and STM (Figure 2d,g), resembling Namibian fairy circles.<sup>46</sup> Similar features were never observed upon grafting the monocomponent systems, nor upon grafting both compounds sequentially (Figure S1). This stimulated us to investigate this intriguing phenomenon in more detail.

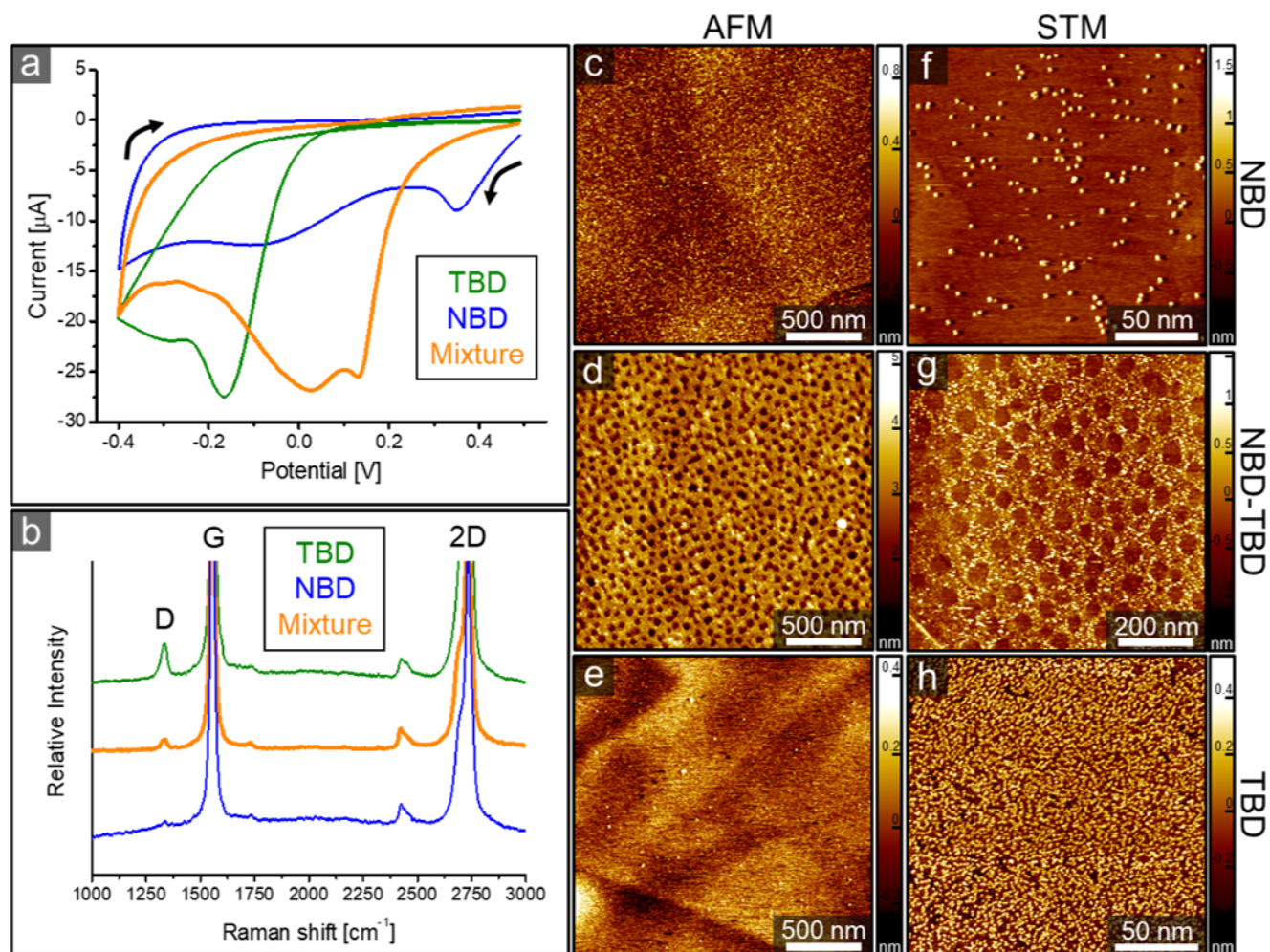


**Figure 2.** (a) Cyclic voltammogram showing each first cycle (from +0.5 V to -0.4 V vs. Ag/AgCl; scan rate, 50 mV/s) of grafting pure 1 mM TBD (green), pure 1 mM NBD (blue) and a mixture (1:1 ratio) of

NBD and TBD (orange) on an HOPG substrate. Arrows indicate the forward and reverse scan direction. (b) Corresponding Raman spectroscopy measurements show distinct relative intensity ratios between the D-peak at  $1335\text{ cm}^{-1}$  and the G-peak at  $1580\text{ cm}^{-1}$ . The resulting  $I_D/I_G$  ratios were as follows: for NBD  $0.022 \pm 0.001$  (blue), for TBD  $0.089 \pm 0.024$  (green) and an intermediate value for the mixed grafting  $0.042 \pm 0.028$  (orange). (c) AFM image after grafting of pure NBD, showing a uniformly packed surface. (d) AFM image after grafting a mixture (1:1 ratio) of NBD and TBD, indicating the formation of circular corrals approximately 50 nm in diameter. (e) AFM image after grafting pure TBD, showing a uniformly covered surface. (f) STM topography image after grafting pure NBD, showing a low density of grafts, attributed to dendritic multilayer formation ( $V_b = -0.4\text{ V}$ ,  $I_t = 100\text{ pA}$ ). (g) STM topography image after grafting of a mixture of NBD and TBD (1:1 ratio), indicating circular bare substrate regions surrounded by densely packed functionalized areas ( $V_b = -0.8\text{ V}$ ,  $I_t = 90\text{ pA}$ ). (h) STM topography image after grafting pure TBD showing a very densely packed layer ( $V_b = -0.6\text{ V}$ ,  $I_t = 200\text{ pA}$ ).

### **Varying the ratio of diazonium precursors.**

In a first series of experiments, we investigated the impact of varying the NBD:TBD concentration ratio (5:1; 3:1; 1:1; 1:3; 1:5) in the grafting solution on the surface morphology, while maintaining a total concentration of 1 mM. Figure 3 shows characteristic CVs, AFM and STM images and Raman spectroscopic data for these different [NBD]:[TBD] ratios. The cyclic voltammograms, as a function of the [NBD]:[TBD] ratio, show a clear trend between that of pure NBD and that of TBD, that can be explained through a variation of the effects discussed in the previous section for the 1:1 mixture. A decay of  $I_D/I_G$  is observed with increasing proportions of NBD (Figure 3b-d). The increasing  $I_D/I_G$  ratio observed with growing corral dimensions is explained by the high-density grafting nature of TBD (Figure 2h) as compared to NBD (Figure 2f). The incorporation of more grafting defects due to increased content of TBD in the grafted regions for larger corral sizes compensates for the lack of defects in the ungrafted regions, thus resulting in an  $I_D/I_G$  increase. In all cases, the surface coverage is non-homogenous. There is a quasi-periodic pattern of grafted and non-grafted areas. However, there are clear differences in surface topography between the different grafting conditions. The larger the TBD content, the lower the total grafted area, and the larger the average corral diameter (Figure 3e-n). A quantification

of this effect is shown in Figure S2. For the largest TBD content, adjacent corrals get interconnected. When further increasing the TBD content an eventual disappearance of the corrals is observed resulting in a fully grafted surfaces when approaching nearly pure TBD grafting solutions (Figure S3).

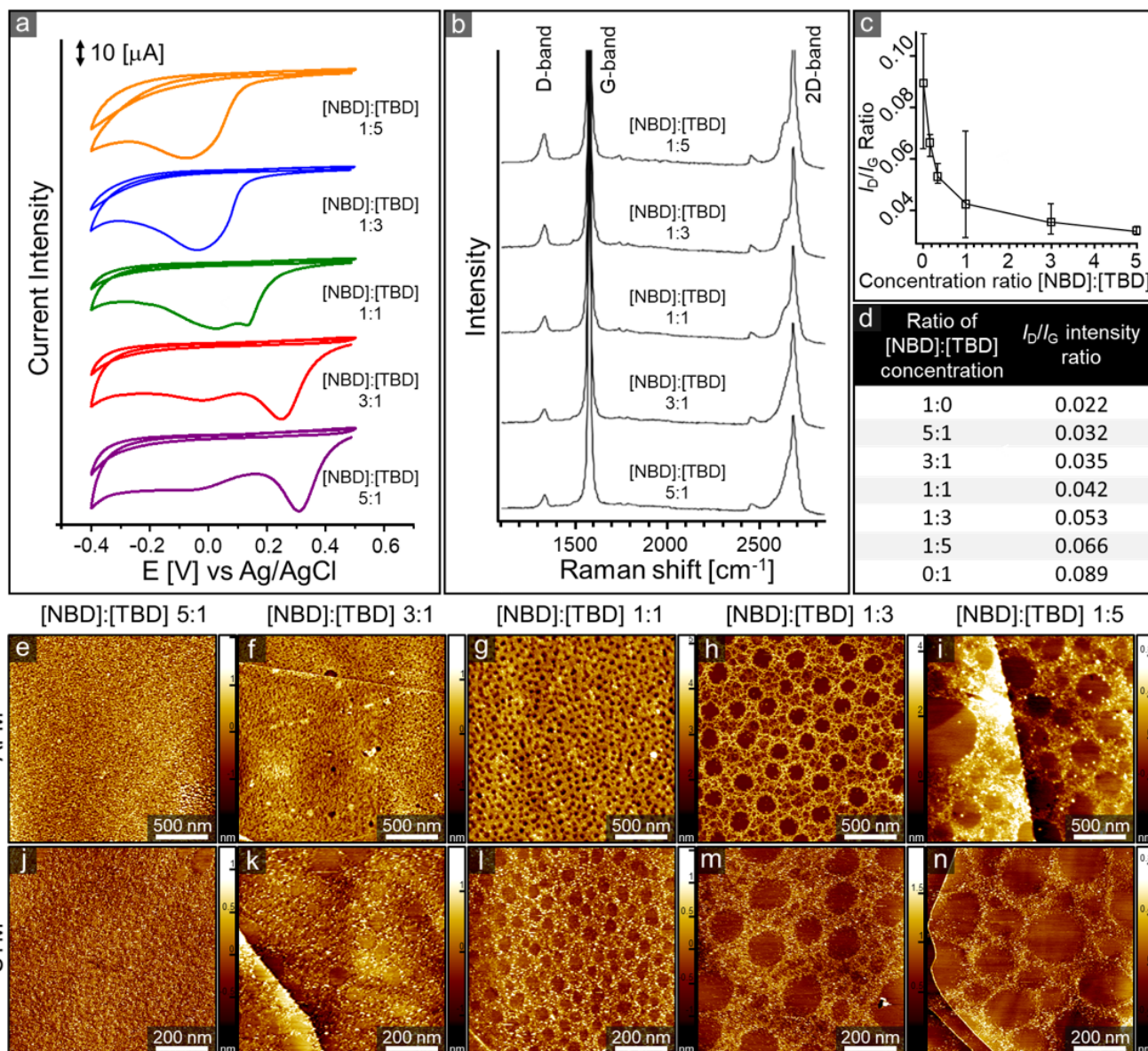


**Figure 3.** (a) Cyclic voltammograms showing the first and second cycle (from +0.5 V to -0.4 V vs. Ag/AgCl, at 50 mV/s) for HOPG in NBD-TBD mixtures at diverse ratios (from 5:1 to 1:5) with a total NBD + TBD concentration of 1 mM. A reductive peak is observed for TBD between 0.0 V and -0.1 V and for NBD between +0.3 V and +0.1 V. (b) Corresponding Raman spectra after grafting varying ratios of NBD:TBD. (c) Raman  $I_D/I_G$  ratio vs. concentration ratio [NBD]:[TBD]. (d) Raman  $I_D/I_G$  ratio vs. concentration ratio [NBD]:[TBD] including values for pure NBD and TBD. AFM images of increasing

ratios of NBD-TBD from 5:1 to 1:5 are shown in (e) 5:1, (f) 3:1, (g) 1:1, (h) 1:3 and (i) 1:5. (j-n) STM topography images follow a similar trend in pore diameter as observed for the corresponding AFM images. STM images were obtained using the following scanning parameters: (j)  $V_b = -0.55$  V,  $I_t = 170$  pA, (k)  $V_b = -0.6$  V,  $I_t = 120$  pA, (l)  $V_b = -0.8$  V,  $I_t = 90$  pA, (m)  $V_b = -0.6$  V,  $I_t = 120$  pA, (n)  $V_b = -0.8$  V,  $I_t = 100$  pA.

### Varying the total concentration of diazonium precursors.

To monitor the effect of the concentration of the grafting solution on the surface morphology, for a constant molar ratio of both grafting components (1:1), a total concentration ranging from 0.25 to 4mM (Figure 4) was investigated. Histograms of the size distribution of the corrals at the different concentrations do not reveal a significant trend (Figure S4). Only for concentrations lower than 2mM these histograms could be constructed, as for the higher concentration it became difficult to identify individual corrals due to high degrees of interconnectivity as the borders between pores became less distinct. For the lower concentrations (0.25 mM, 0.5 mM and 1.0 mM), the average corral diameter measures  $70 \pm 10$  nm,  $70 \pm 10$  nm and  $50 \pm 8$  nm, respectively. In contrast to corral diameter, a clear trend was observed in the surface coverage of the corrals, independent on whether they are interconnected or not. Figure S4 shows that the surface coverage of corrals increases from about 10% at 0.5 mM to 50% at 4 mM.

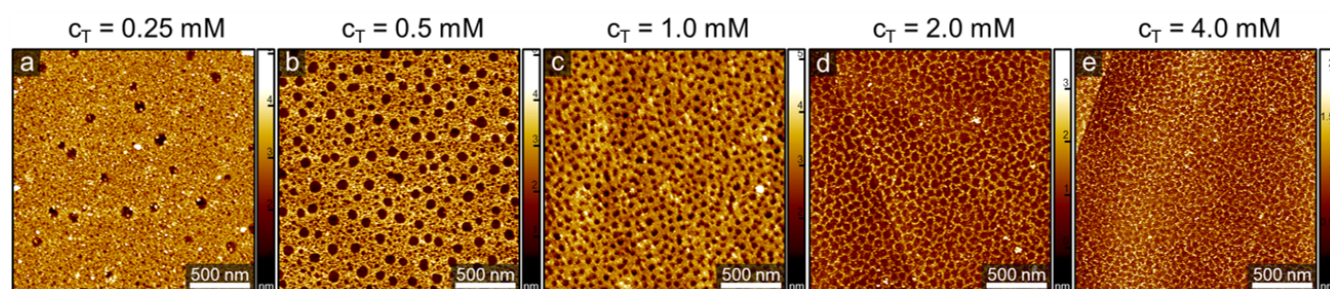


**Figure 4.** AFM topography images of grafting using cyclic voltammetry on HOPG while varying the total concentration of NBD + TBD yet maintaining the 1:1 ratio. Total concentrations were varied from (a) 0.25 mM to (e) 4.0 mM and show no apparent trend in corral diameter. However, the total surface coverage of corrals clearly increases with increasing concentration.

### **Electrochemical control over nanostructured grafting.**

While the concentration and ratio dependent grafting protocols show clearly observable trends in the corral size and their surface coverage, the CV approach is somewhat limited, due to sometimes significant variations from session to session. An experienced operator though can reach a success rate of about 70-80%. Therefore, we also explored an approach based on chronoamperometry (CA). In the original CV procedure, the electroreduction of diazonium mixtures was accomplished by sweeping over a wide range of potentials, scanning (from +0.5 V to -0.4 V vs. Ag/AgCl). The irreversible reduction peak for NBD is broader and situated at less negative potentials than that of TBD (Figure 2a). The fact that these reduction waves only partially overlap, suggests it is possible to fine tune the radical generation process by selecting the reduction potential. Changing the selected reduction potential is expected to affect the relative amount and speed by which NBD or TBD are reduced, hopefully yielding even better control over the coverage and morphology of the grafted adlayer.

Figure 5 shows the AFM morphology of the nanocorrals patterned HOPG surface formed at different applied potentials while keeping all other parameters (concentration, [NBD]:[TBD] ratio, grafting time) fixed. At +0.3 V (and above), the surface remains pristine; at +0.2 V, some random grafting (without the formation of nanocorrals) occurs; while at more negative potentials the corrals are formed, varying in size and density for different reduction potentials. This observation can be explained as follows: at +0.3 V, neither NBD nor TBD are electrochemically reduced, hence there is no grafting at this potential; at +0.2 V, NBD can already be reduced, but not TBD, yielding low-density randomly grafted HOPG; at +0.1 V and more negative potentials, both NBD and TBD can be reduced, leading to nanocorral formation. This CA grafting protocol was also applied on various types of CVD graphene (SiO<sub>2</sub>, Pt(111) and Pt foil). For some cases, unique alignment (Pt(111)) or shape distorted corrals (Pt foil) were observed, originating from the directing properties of the underlying substrate (Figure S5).<sup>44</sup>

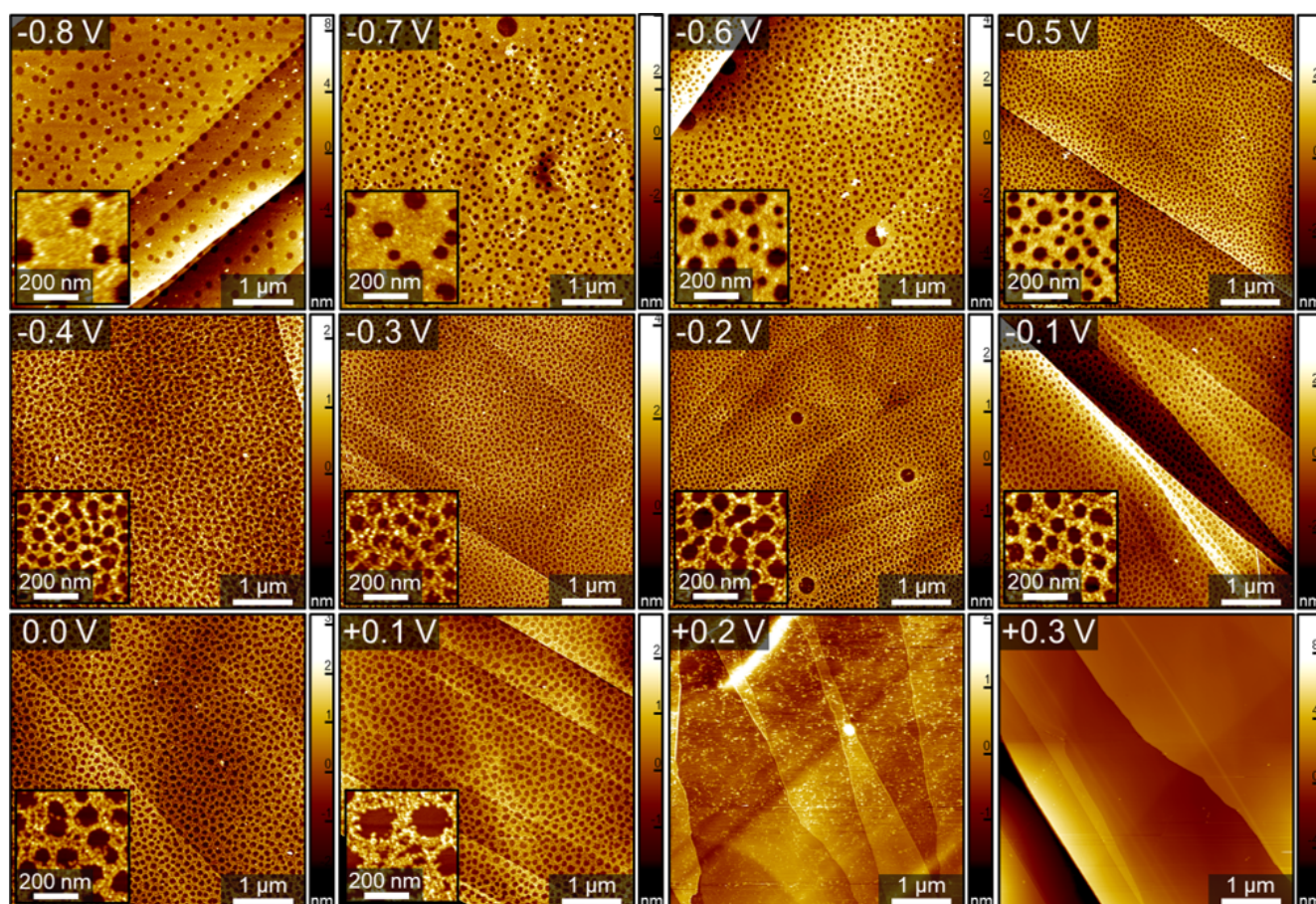


**Figure 5.** AFM topography images of HOPG substrates grafted with a 1:1 mixture of NBD and TBD (total concentration of 1 mM) for 60s using chronoamperometry (CA) at different potentials (vs. Ag/AgCl). Insets provide a detailed zoom of the sample surface. At potentials of and exceeding +0.2 V no well-defined corrals are formed. From +0.3 V onwards, no grafting was observed.

A quantitative analysis of the relationships between the dimensions / the surface density of nanocorrals and the applied electrochemical potential is given in Figure 6. To construct Figure 6a, the corrals were assumed to have a perfectly round shape and calculated surface areas were converted to corral diameters. The average ‘diameter’ of corrals is the largest (~130 nm) at +0.1 V and the lowest (~45 nm) at -0.5 V, then increases again for more negative potentials. Interestingly, the dependency for the surface density of corrals is not monotonic either: with ~20 corrals per  $\mu\text{m}^2$  at +0.1 V, going through a maximum (~125 of corrals per  $\mu\text{m}^2$ ) at -0.5 V, then decreasing at more negative potentials. The total pore coverage of bare HOPG starts at ~23 % for +0.1 V and gradually increases until a maximum of ~28

% is reached at -0.2 V and declines with applying even more negative potentials (Figure 6b). Both trends are reproducible and can be used for the preparation of nanocorrals-decorated HOPG samples.

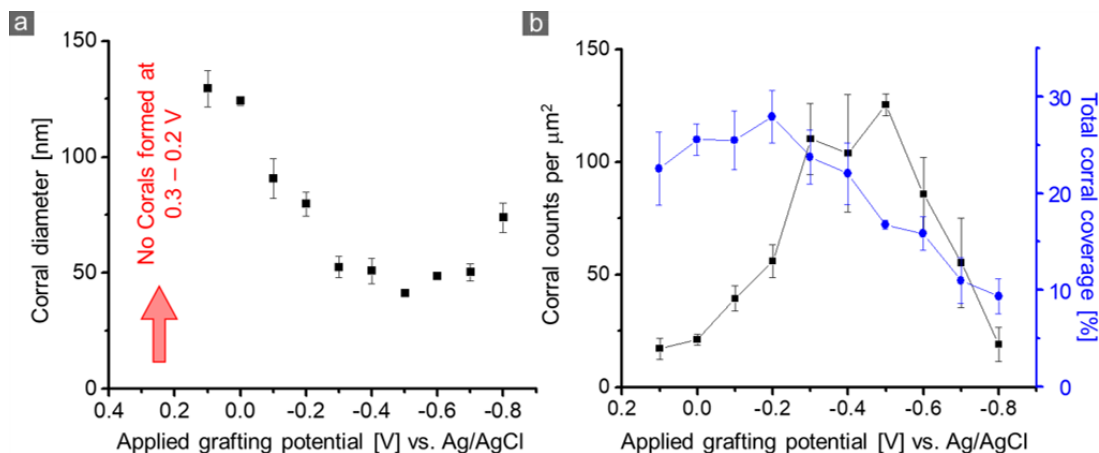


**Figure 6.** Quantification of (a) corral diameter and (b) corral density versus applied grafting potential with total corral coverage using the CA approach at different applied potentials. A minimum in corral diameter (45 nm) is observed between -0.3 V and -0.7 V. For the corral density a maximum can be observed between -0.3 V and -0.5 V while the total corral coverage reaches a maximum (~28 %) at -0.2 V and decreases towards more negative potentials. Data for both graphs was obtained using the Particle and Pore analysis function available in the SPIP software. Thresholds were determined as half the height of the grafted layers. Only fully resolved corrals were considered for constructing the corral diameter vs. applied grafting potential graph. Three  $25 \mu\text{m}^2$  images, obtained at different locations were used for analysis of corral diameter and corral counts per  $\mu\text{m}^2$ .

### Covalent nature and composition of the observed nanopatterns.

Several elements support the hypothesis that the nanostructured surfaces are functionalized *via* covalent bonds, rather than physisorption. The nanostructured surfaces are not affected by thorough rinsing protocols. However, the strongest evidence comes from Raman spectroscopy and microscopy, and STM imaging. As discussed before, the appearance of the D band in the Raman spectra is good evidence for the formation covalent of bonds. Moreover, the spatial resolution provided by Raman microscopy allows clear differentiation between the grafted areas and the nanocorrals (Figure 7a). The intensity of the D band, characteristic for grafting, is significantly lower in the corrals (Figure 7b). High

resolution STM imaging shows a typical<sup>24</sup> distortion of the graphite lattice in the immediate vicinity of the grafting sites (Figure 7d).

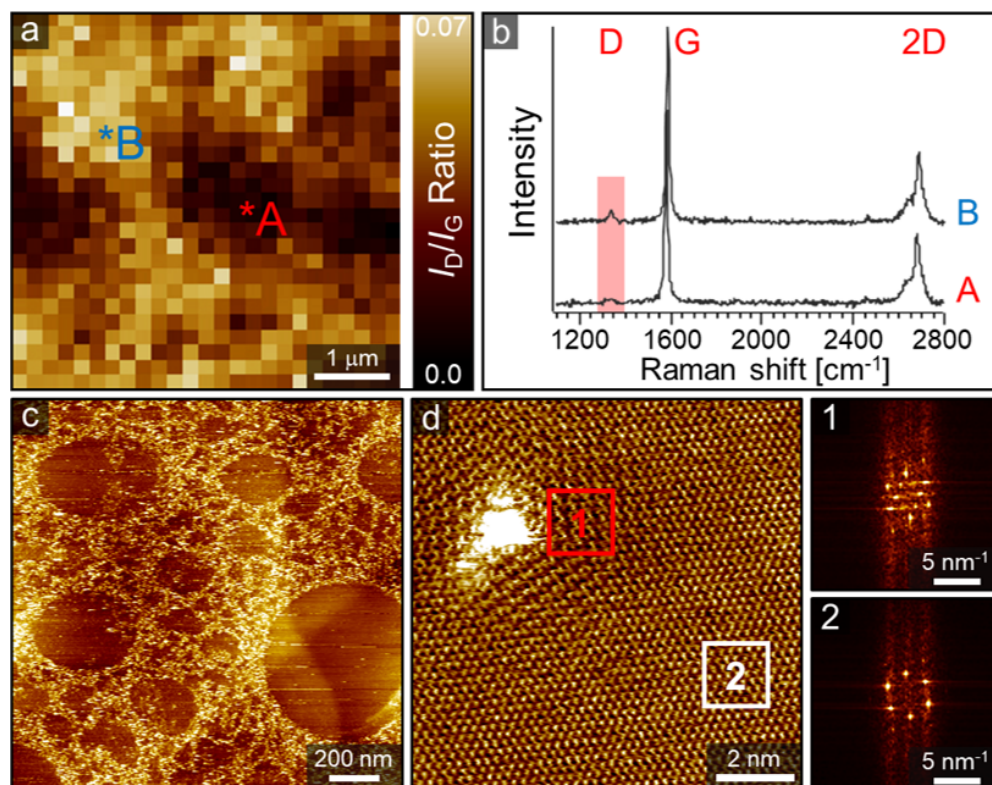


**Figure 7.** (a) Raman spectroscopy mapping was used to generate an  $I_D/I_G$  map, visualizing locations of higher (B) and lower (A) degrees of functionalization of a sample surface prepared according to slightly modified protocol to maximize corral size. A 1:5 ratio [NBD]:[TBD] (1 mM) was grafted by a modified CV protocol where three consecutive scans from +0.5 V to -0.4 V were paused at +0.2 V for 5 minutes, only during the first cycle. This resulted in large corrals that were observable by Raman mapping. (b) Corresponding Raman spectra A and B as obtained by the Raman mapping experiment in panel(a). (c) STM topography image of a 1 mM NBD+TBD (1:5 ratio) grafted sample using the modified CV approach in order to maximize the corral size ( $V_b = -0.4$  V,  $I_t = 150$  pA). (d) High resolution STM image of a single covalently bound molecule ( $V_b = -0.01$  V,  $I_t = 200$  pA). FFT analysis (1) and (2) shows that the graphite lattice appearance is distorted in the direct vicinity of the graft.

For NBD we have previously proven<sup>24</sup> covalent attachment of the aryl units grafted on graphene on copper using X-ray photoelectron spectroscopy (XPS), which revealed both C-sp<sup>3</sup> and C-N components after deconvolution of the observed band. Because of the all-carbon nature of grafted TBD,

XPS is of little use to probe its surface coverage. However, XPS reveals unambiguously that NBD is grafted on the surface, and that the higher the proportion of NBD in mixtures of NBD+TBD, the more NBD is grafted. The level of NBD modification in the mixed spectra is much lower than in the NBD reference sample: 1.2% nitrogen is detected in the TBD:NBD 1:3 sample, compared to 6% nitrogen in the pure NBD sample (Figure S6-S10).

### **Mechanistic considerations.**

The exact mechanism of nanocorral formation has not been fully determined yet. The determination is hindered by the threefold complexity of the grafting system: 1) *multi-component variable composition* (including unstable  $\text{HNO}_2$  and two diazonium salts), 2) *high heterogeneity* ( $\text{N}_2$  and NO gases, aqueous solution, solid hydrophobic graphite, and water-insoluble decomposition products), and 3) *simultaneous non-equilibrium processes* (electrochemical reduction and chemical decompositions leading to the formation of potential nanobubbles, precipitates, physisorbed and chemisorbed adlayers on the HOPG surface). Our best working hypothesis is based on the formation of stabilized nanobubbles at the graphite-solution interface (Figure 8). Below we rationalize different aspects of this hypothesis.

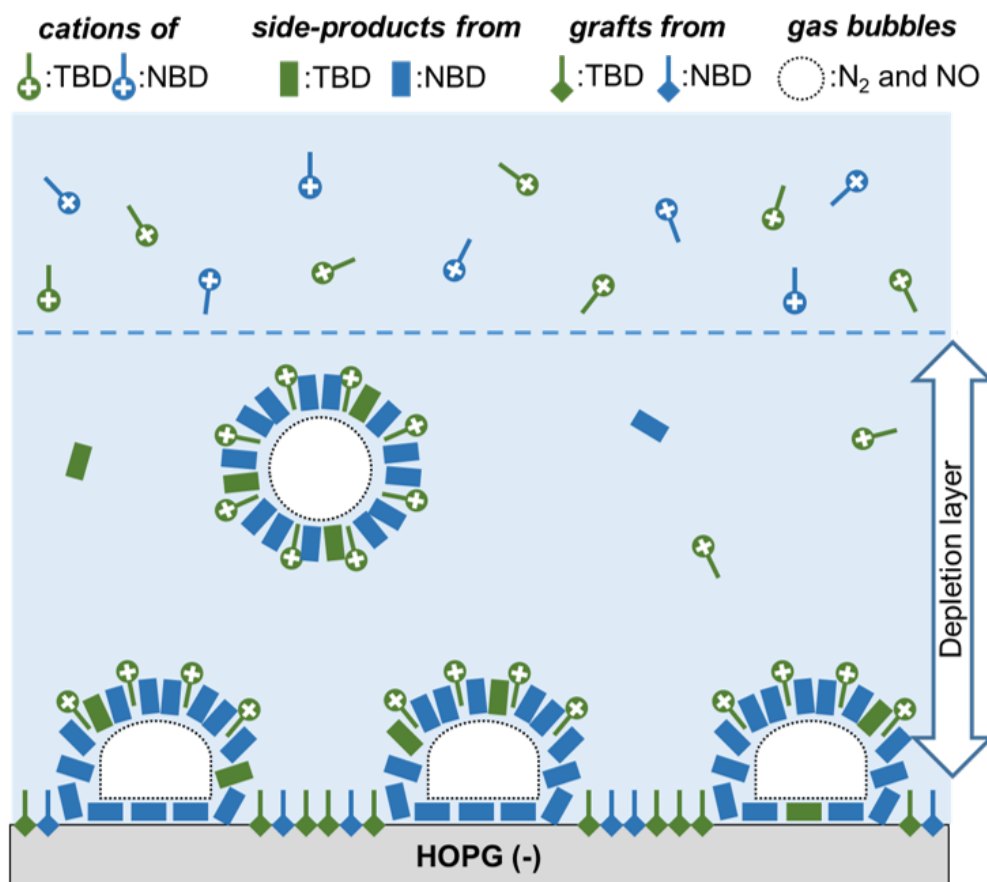


**Figure 8.** Schematic representations of stabilized nanobubbles formed within the electrochemical depletion layer that are hypothesized as responsible for the patterned substrate surface protection from the grafting by aryl radicals.

$N_2$  (from decomposition of diazonium salts) and NO (from  $HNO_2$ ) are the only gases that are generated during grafting. The first hint that nanobubbles might be responsible for nanocorrals formation came from control experiments in which increasing only the concentration of  $HNO_2$  systematically increased the diameter of nanocorrals (Figure S11). Among dedicated studies about nanobubbles at interfaces<sup>47</sup> the most relevant example is the direct observation of interfacial nanobubbles on the HOPG surface when the gas ( $N_2$ ) was chemically generated from  $NH_4Cl$  and  $NaNO_2$ .<sup>48</sup> In our case, large visible bubbles on the HOPG surface can be easily observed after grafting (Figure S12a), but unfortunately,

short reaction times preclude *in-situ* nanoscale visualization of graphite-solution interface during nanocorrall formation, and hence, the intermediate formation of nanobubbles can be only postulated.

Simultaneously with the generation of gases, large quantities of water-insoluble organic residues are produced from the diazonium salts (Figure S12b). Indeed, only a minor fraction of diazonium salts results in aryls covalently grafted onto the HOPG. The rest decomposes into poorly soluble side-products (phenols, biphenyls, *etc.*),<sup>49</sup> that, due to their hydrophobic nature, get displaced to 1) graphite-solution, 2) N<sub>2</sub>/NO-solution or 3) air-solution interfaces. The direct observation of round physisorbed aggregates was possible in control EC-STM experiment (Figure S13). Effectively, particulates at the N<sub>2</sub>/NO – solution interface should improve the structural stability of nanobubbles. Such organic residue can be also seen in AFM images of nanocorralls if the substrate was washed only with water (Figure S14). That is why in our optimized protocol washing with organic solvent is included to completely remove all physisorbed species from the patterned substrate.

The third important component, crucial for the reproducible electrochemical formation of nanocorralls, appears to be the use of two diazonium salts. Rarely observed corralls in pure TBD or NBD systems were highly irregular in size and surface distribution (Figure S15). In 2016, Cui *et al.* presented AFM images of circular structures similar in appearance to our corralls.<sup>50</sup> The authors claimed that those structures are the result of *p*-carboxyphenyldiazonium assisted electrochemical etching of HOPG. Our experiments with this mono-component system did not reproduce such results; instead, random grafting similar to the films produced in pure NBD was observed (Figure S16). And only when a mixture of two different diazonium salts was exposed to CV or CA grafting nanocorralls were formed (Figure 2-5). This can be understood if we consider 1) amphiphilic character of the diazonium salts and 2) specifics of electrochemical reduction: a micrometers-thick depletion layer is formed over a milliseconds time scale when starting the electrochemical procedure. In this layer the most reactive diazonium salt (*i.e.* NBD) is completely reduced and can be replenished only *via* diffusion from the solution outside the depletion

layer. Thus, the fast generation of gases and precipitates within the whole volume of the depletion layer synchronizes nanobubble formation, while the remaining intact molecules of the less reactive diazonium salt act as amphiphiles that stabilize all heterogeneous interfaces (between solids, the solution and gases). Furthermore, the Columbic repulsion between positively charged shells of nanobubbles can also explain quite uniform distribution of nanocorrals on the negatively polarized HOPG surface. Within the presumed mechanism of stabilized nanobubbles at the solid–liquid interface, that subsequently act as a mask for radical grafting of the locally wetted parts of the HOPG surface, all factors that influence the shape and size of these bubbles before the incoming radicals “fixate” the interfacial morphology will affect the result: bubble nucleation and growth,<sup>45</sup> equilibrium bubble shape and contact angle, and effects of static friction at the solid–liquid interface.<sup>51</sup> The most abundant nanocorral for any given set of experimental conditions (solution composition, electrochemical reduction rate) will reflect both the thermodynamic and kinetic situation in a convoluted manner. Figure 8 represents a graphical summary of the discussed structures.

In summary, the roles of NBD (*i.e.* the most electrochemically active diazonium salt) for the nanocorral formation are 1) source of N<sub>2</sub>, 2) source of insoluble side products, 3) surface grafting, while not-yet-reduced molecules of the second diazonium salt (*i.e.* TBD) function also as 4) ionic amphiphiles. In order to promote reproducible formation of nanocorrals the last function seems to be particularly important. For a grafting system using single diazonium salt this could be potentially achieved by introduction of electrochemically stable ionic amphiphile or by using controlled chemical reduction (that unlike electrochemical reduction, will not cause the formation of depletion layer in the vicinity of graphite surface). Both strategies are currently investigated in our group.

Finally, we highlight that the chemical structure of diazonium salts not only affects their reduction potential but also can define the shape of nanocorrals. The round shape of nanocorrals implies minimal anisotropy of adsorbate-substrate interactions, which can be understood considering the bulkiness of

TBD *tert*-butyl groups and the structural variability of side products from NBD (due to radical attacks of its aromatic core).<sup>52,53</sup> There is no preferred orientation of molecular adsorbates on HOPG and hence interfacial bubbles adopt hemispherical shapes resulting in circular nanocorrals. Different diazonium precursors can yield elongated nanocorrals with straight linear edges (Figure S17) – presumably, due to higher crystallinity and hence anisotropy of supramolecular structures formed at HOPG-solution interface. The systematic study of other grafting combinations is still under investigation and will be reported in time.

### **Nanocorrals for nanoconfined self-assembled molecular network formation.**

The typical quasi-periodic pattern of nanocorrals we obtain may serve several purposes. Each of these nanocorrals can be considered as a small substrate of defined size and shape, isolated from the millions of nanocorrals surrounding it. Here we demonstrate that they can be used to confine supramolecular assemblies and even as 2D nanoreactors for chemical transformations. Supramolecular self-assembly in these nanocorrals can be achieved at the liquid-solid interface, as is demonstrated for 10,12-pentacosadiynoic acid (PCDA, Figure 9). Once a “fairy circle” substrate is exposed to a solution of PCDA (100 × dilution from saturated solution) in toluene, periodic features appear in some of the nanocorrals. The supramolecular ordering consists of rows of molecules stacked in parallel, called lamellae. The brightest features of these molecules in the nanocorrals relate to the diacetylene units, which are tilted with respect to the alkyls. The darkest and thinnest rows correspond to the meeting of the methyl ends of the molecules, whereas the alternating rows of intermediate contrast are assigned to the regions of hydrogen bonding of the carboxyl groups. This molecule self-assembles in nanocorrals in a fashion resembling its behavior on unfunctionalized graphite (Figure S18).<sup>36,54-56</sup> Comparing the orientation of molecules in different nanocorrals indicates that they are rotated by nearly 60° or 120°, reflecting the templating role the graphite substrate plays in directing the orientation of the molecules,

*i.e.* the alkyl chains run preferentially parallel to one of the main symmetry axes of graphite. The lack of any other correlation in the orientation of PCDA domains between adjacent corrals suggests that monolayer nucleation and growth occur independently in each of the nanocorrals, but more in-depth studies are required. Next, we set out to use these corrals as nanoreactors. Upon applying UV light to PCDA filled corrals, a topochemical polymerization reaction is induced.<sup>57,58</sup> The resulting polydiacetylene chains are readily distinguished in the STM images as very bright lines (Figure 9). Naturally, given the confined nature of monomeric units, the maximum polymer length is limited and determined by the nanocorral dimensions.<sup>54,59</sup> The size-tunability of these corrals can thus be exploited to control the polydispersity of chemical reactions.

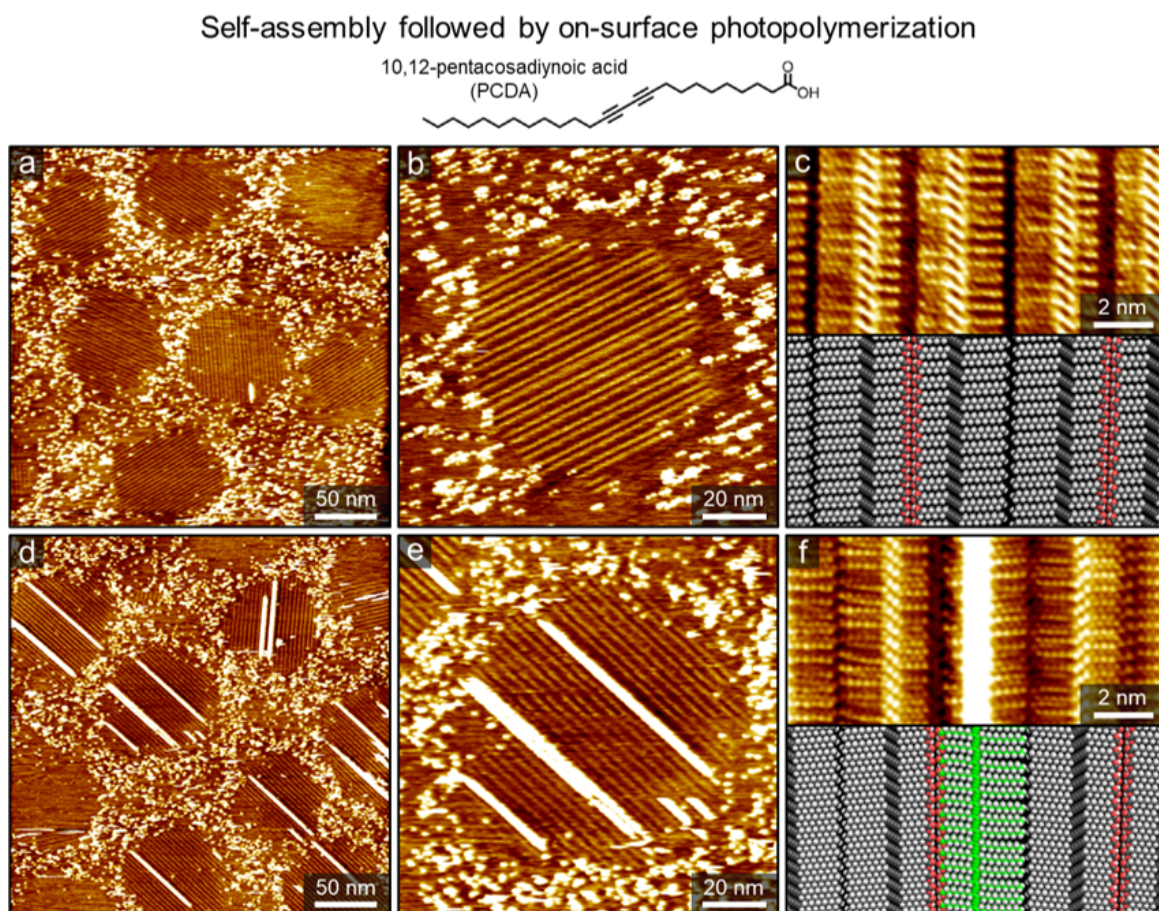


**Figure 9.** (a) STM topography images demonstrating the confined molecular self-assembly of 10,12-pentacosadiynoic acid at the liquid-solid interface inside the nanocorrals ( $V_b = -0.8$  V,  $I_t = 60$  pA). (b) High resolution zoom of a single corral containing a single domain of self-assembled PCDA molecules

( $V_b = -0.8$  V,  $I_t = 60$  pA). (c) Top: molecular resolution STM image of self-assembly at the liquid/solid interface from a saturated PCDA solution in 1-phenyloctane on pristine HOPG ( $V_b = -0.8$  V,  $I_t = 100$  pA). Bottom: tentative molecular model matching the observed structure. (d) STM topography image acquired following the photopolymerization. The appearance of very bright strands indicates a successful polymerization of adjacent PCDA molecules ( $V_b = -0.9$  V,  $I_t = 50$  pA). (e) Zoom of a single corral after photopolymerization ( $V_b = -0.9$  V,  $I_t = 50$  pA). (f) Top: molecular resolution STM image of a pulse induced polymerized PCDA chain at the liquid/solid interface using a saturated PCDA solution in 1-phenyloctane on pristine HOPG ( $V_b = -0.5$  V,  $I_t = 300$  pA). Bottom: tentative molecular model corresponding to the polymerized structure.

## Conclusions

A bottom-up approach has been developed for the formation of nanoconfined spaces on substrates such as graphite or graphene. Electrochemically activated dediazotization of a mixture of two aryl diazonium compounds leads to nanostructured grafted graphitic surfaces. A quasi-periodic pattern of graft-free islands (*i.e.* nanocorrals) is formed. The diameter of nanocorrals can be tuned by controlling the electrochemical activation conditions and the ratio between both diazonium compounds. Concentration has an impact on the island density. The formation of these nanocorrals likely involves the generation and stabilization of nanobubbles. We demonstrate that the nanostructured graphitic surfaces can for instance be used as templates for the nanoconfined formation of self-assembled molecular networks and for on-surface reactivity. The simultaneous formation of a large number of these nanocorrals will make it possible to investigate nanoconfinement effects in a statistically sound approach. Furthermore, this nanostructured grafting may also be of interest to impact the electronic properties of graphene.

## EXPERIMENTAL

### Materials

4-Nitrobenzenediazonium (NBD) tetrafluoroborate (97%), p-Aminobenzoic acid (>99%), 10,12-pentacosadienoic acid (PCDA, 97%), 1-octanoic acid (99%), toluene (spectroscopic grade), 1-phenyloctane (98%) and analytical grade hydrochloric acid (HCl) were purchased from Sigma-Aldrich, 3,5-bis-*tert*-butylaniline (TBD) (98%) was purchased from TCI-Tokyo Chemical Industry Co., Ltd. All compounds were used without further purification. As graphite substrates, 12x 12 mm<sup>2</sup> pieces of highly oriented pyrolytic graphite (HOPG) (ZYB grade, Momentive Performance Materials) were used.

### **Electrografting**

All cyclic voltammetry measurements were performed using the Autolab PGSTAT101 Potentiostat (Metrohm Autolab BV, Netherlands). Prior to each experiment, the HOPG electrode was freshly cleaved using scotch tape. The electrochemical modification of the HOPG sample was carried out in a home-built single-compartment three-electrode cell, with a working electrode surface area of 50.3 mm<sup>2</sup>, Pt wire counter electrode and Ag/AgCl/3M NaCl reference electrode. All potentials are reported *versus* this reference. Freshly cleaved HOPG substrates mounted in the electrochemical cell were exposed to 5 ml supporting electrolyte (50 mM aqueous HCl) containing 4-nitrobenzenediazonium (NBD), 3,5-bis-*tert*-butylbenzenediazonium (TBD) or a mixture of both with a total concentration of 1 mM (or as stated otherwise). TBD was generated *ex tempore* from its more stable 3,5-bis-*tert*-butylaniline form by adding a small excess (100  $\mu$ l) of 0.1 M aqueous NaNO<sub>2</sub> to the calculated volume of 1 mM, followed by stirring for 2 minutes. For the preparation of mixtures, after 90 seconds this solution was mixed thoroughly with the ratiometric amount of 1 mM solution of the other diazonium compound to achieve a total volume of 5 ml. The NBD and TBD solutions, or their mixtures, were subsequently transferred to the electrochemical cell, 30 seconds after mixing. For all solutions used in this work, high purity water (Milli-Q, Millipore, 18.2 M $\Omega$  cm, TOC < 3 ppb) was used throughout.

Two particular electrografting protocols were employed on HOPG and graphene: cyclic voltammetry (CV) and chronoamperometry (CA). In the CV protocol, the substrate potential was cycled three times between +0.5 V to -0.4 V at 50 mV/s, starting at the most positive potential. This protocol was used to

test the effect of varying [NBD]:[TBD]ratio(5:1, 3:1, 1:1, 1:3 and 1:5) at a fixed total NBD and TBD concentration ( $C_{\text{NBD}}+C_{\text{TBD}}= 1 \text{ mM}$ ), and the effect of varying the total concentration of diazonium ( $C_{\text{NBD}}+C_{\text{TBD}}= 0.25 \text{ mM}, 0.5 \text{ mM}, 1 \text{ mM}, 2 \text{ mM}, 4 \text{ mM}$ ) for a fixed ratio (1:1). The CA protocol was used to study potential dependent nanocorral formation, while the NBD to TBD ratio (1:1) and total concentration ( $C_{\text{NBD}}+C_{\text{TBD}}= 1 \text{ mM}$ ) were kept constant. Electrochemical potentials ranging from +0.3 V down to -0.8 V were applied for 60 seconds. To remove physisorbed grafting residues and other unreacted species, samples were thoroughly washed with Milli-Q water, hot toluene (90 °C) and rinsed with Milli-Q-water again before drying with a gentle stream of argon.

**Self-assembly and polymerization:** A saturated PCDA/toluene stock at room temperature (21 °C) was 100 times diluted before dropcasting onto the functionalized HOPG surface. The droplet was left to evaporate overnight in a closed glass Petri dish filled with a toluene saturated atmosphere to prolong the time available for molecular self-assembly of the PCDA molecules. The samples were dried with a gentle stream of argon once removed from the Petri dish. UV irradiation was used to initiate the polymerization (300 W, Max 303 Xenon light source with low pass filter to transmit only wavelengths below 300 nm, Asahi Spectra, Japan). Samples were illuminated at 10 % of the maximum power output approximately 1.5 cm distance from the surface for two hours unless stated otherwise.

**Raman spectroscopy:** Raman measurements were performed with an OmegaScope™ 1000 (AIST-NT). Laser light (632.8 nm) from a He-Ne laser was focused onto the sample surface from the side (with an angle of 28° to sample surface) and top, for 'grating' and 'normal' measurements, respectively, through an objective (MITUTOYO, BD Plan Apo 100x, N.A. 0.7). Irradiance at sample surface was about 500 kW/cm<sup>2</sup>. Raman scattering was collected with the same objective and directed to a Raman spectrograph (Horiba JY, iHR-320) equipped with a cooled-charge coupled device (CCD) camera operated at -100 °C (Andor technology, DU920P-BRDD) through a pinhole, a dichroic mirror (Chroma Technology Corporation, Z633RDC) and long pass filter (Chroma Technology Corporation, HQ645LP).

Accumulation time for each point in 'grating' measurement was 1 second. All the measurements were carried out under ambient conditions and at room temperature.

**Scanning tunneling microscopy (STM):** All STM experiments were conducted in ambient conditions (temperature: 20–23 °C; humidity: 40%–50%) using a PicoLE system operating in constant current mode. STM tips were mechanically cut from Pt/Ir (80% / 20%, diameter: 0.25 nm) wire. Freshly cleaved or covalently modified highly oriented pyrolytic graphite (CM-HOPG) (grade ZYB, Advanced Ceramics Inc., Cleveland, OH, USA) substrate was used. STM data analysis was executed using Scanning Probe Imaging Processor 6.3.5 software (SPIP, Image Metrology ApS). Scanning parameters are indicated in figure captions and expressed as  $V_b$  for the sample bias and  $I_t$  for the tunneling current.

**Electrochemical scanning tunneling microscopy (EC-STM):** All EC-STM experiments were carried out with an apparatus designed at the University of Bonn as described elsewhere.<sup>60</sup> In order to eliminate the influence of oxygen as well as acoustic and electromagnetic interference, the entire EC-STM system is housed in a sealed aluminum chamber with electrical and liquid feedthroughs and filled with Ar. The STM tips were electrochemically etched from 0.25 mm tungsten wire in 2 M KOH solution, rinsed with Milli-Q water, dried and subsequently coated by passing the tip through a lamella of hot-melt glue. The used setpoint current  $I_t$  and bias voltage  $V_b$  are mentioned in the figure captions.

**Atomic force microscopy (AFM):** All AFM images were recorded in tapping mode at the air/solid interface at minimized forces using AC160TS-R3 probes (spring constant  $\sim 26$  N/m) at a resonance frequency of  $\sim 300$  kHz from Olympus Corporation. All samples created by the cyclic voltammetry approach were imaged using a Cypher ES system from Asylum Research at 32 °C. The samples produced by chronoamperometry were imaged using a MultiMode 8 system from Bruker. Data analysis was executed using Scanning Probe Imaging Processor 6.3.5 software (SPIP, Image Metrology ApS)

**X-ray photoelectron spectroscopy (XPS):** Spectra were recorded on a Kratos Axis Supra X-ray Photoelectron Spectrometer employing a monochromated Al K $\alpha$  ( $h\nu = 1486.7$  eV, 5 mA emission) X-ray source, hybrid (magnetic/electrostatic) optics with a slot aperture, hemi-spherical analyzer,

multichannel plate and delay line detector (DLD). The analyzer was operated in fixed analyzer transmission (FAT) mode with survey scans taken with a pass energy of 160 eV and high-resolution scans with a pass energy of 20 eV. Samples were mounted using conductive carbon tape to ensure electrical contact with the spectrometer. The resulting spectra were processed using CasaXPS software. Binding energy was referenced to the Ag 3d<sub>5/2</sub> peak at 368.21 eV measured under the same operating conditions. Spectra were acquired at emission angles ( $\theta$ ) of 0° (normal emission) and 70°. High resolution spectra were fitted using the “LF( $\alpha$ ,  $\beta$ , w, m,n)” lineshape corresponding to a numerical convolution of Lorentzian functions (with exponents  $\alpha$  and  $\beta$  for the high binding energy and low binding energy sides) with a Gaussian (width m, n times) and inclusion of tail-damping (w) to provide finite integration limits. Details of this line-shape function are available in the CasaXPS documentation online. Carbon 1s sp<sup>2</sup> components in modified HOPG samples were based on an experimentally acquired peak for unmodified HOPG. Tougaard 2-parameter universal backgrounds were fitted to the high-resolution spectra to allow peak fitting. Relative sensitivity factors based on Scofield cross-sections were used for quantification. Escape depth correction was performed according to the approximation of electron attenuation length by Seah. Angular dependency of elastic scattering was discounted. The instrument intensity energy response function (IERF) was determined by calibration using gold, silver and copper standards and the NPL calibration software (National Physical Laboratory, UK). Use of these relative sensitivity factors does not account for any attenuation due to overlayers or other surface contamination and assumes a uniform depth distribution of elements within the information depth of the sample. Matrix effects are also discounted.

## **ASSOCIATED CONTENT**

The Supporting Information is available free of charge on the ACS Publications website at DOI: XXX. including experimental details, corral analysis under different experimental conditions, additional AFM images, optical data, EC-STM data, XPS analyses

## **AUTHOR INFORMATION**

### **Corresponding Authors**

\*phanthanhhai@qnu.edu.vn

\*oleksandr.ivasenko@kuleuven.be

\*steven.defeyter@kuleuven.be

### **ORCID**

Thanh Hai Phan: 0000-0002-6883-7849

Hans Van Gorp: 0000-0002-5983-0143

Yasuhiko Fujita: 0000-0003-1302-1436

Samuel Eyley: 0000-0002-1929-8455

Wim Thielemans: 0000-0003-4451-1964

Stijn F.L. Mertens: 0000-0002-5715-0486

Oleksandr Ivasenko: 0000-0001-9182-3974

Steven De Feyter: 0000-0002-0909-9292

### **Author Contributions**

T.H.P. discovered the phenomenon. T.H.P. and H.V.G. prepared the samples. Y.F. performed Raman analysis. H.V.G. and L.Z. recorded and analyzed the AFM data. T.H.P. recorded the STM data. L.V. and T.M.T.H. investigated molecular self-assembly in nanocorrals. T.H.P. and T.M.T.H. conducted EC-STM experiments. L.V. investigated polymerization in the nanocorrals. S. E. and W. T. performed XPS characterization of the functionalized HOPG. B. H. was involved in discussions. S.F.L.M. analyzed voltammetric and chronoamperometric data. T.H.P., O.I., J.G. and S.D.F. conceived and designed the concepts. T.H.P., H.V.G., O.I. and S.D.F. co-wrote the paper. All authors contributed to the conception of experiments and discussion of the results, and commented on the manuscript.

## Acknowledgement

This work is supported by the Research Foundation Flanders (FWO), FWO under EOS 30489208, and KU Leuven - Internal Funds. The research leading to these results has also received funding from the European Research Council under the European Union's Seventh Framework Programme (FP7/2007-2013)/ERC Grant Agreement No. 340324 to S.D.F. LV. thanks Research Foundation Flanders (FWO) for personal fellowship. T.M.T.H. acknowledges financial support through a Marie Skłodowska-Curie Individual Fellowship (EU project 706564 – NGUEC). S.E. and W.T. acknowledge financial support through the Accelerate3 project from the Interreg Vlaanderen-Nederland program and Flanders Innovation and Entrepreneurship for XPS. W.T. also thanks the Provincie West-Vlaanderen (Belgium) for financial support through his Provincial Chair in Advanced Materials.

## References

1. Sosa-Vargas, L.; Kim, E.; Attias, A.-J. Beyond “Decorative” 2D Supramolecular Self-Assembly: Strategies towards Functional Surfaces for Nanotechnology. *Mater. Horiz.* **2017**, *4*, 570-583.
2. Yu, K. R.; Ricardo, G. Advanced Oxidation Scanning Probe Lithography. *Nanotechnology* **2017**, *28*, 142003.
3. Andrews, A. M.; Liao, W.-S.; Weiss, P. S. Double-Sided Opportunities Using Chemical Lift-Off Lithography. *Accounts Chem. Res.* **2016**, *49*, 1449-1457.
4. Liu, X.; Carbonell, C.; Braunschweig, A. B. Towards Scanning Probe Lithography-Based 4D Nanoprinting by Advancing Surface Chemistry, Nanopatterning Strategies, and Characterization Protocols. *Chem. Soc. Rev.* **2016**, *45*, 6289-6310.
5. Mackus, A. J. M.; Bol, A. A.; Kessels, W. M. M. The Use of Atomic Layer Deposition in Advanced Nanopatterning. *Nanoscale* **2014**, *6*, 10941-10960.
6. Xia, D.; Ku, Z.; Lee, S. C.; Brueck, S. R. J. Nanostructures and Functional Materials Fabricated by Interferometric Lithography. *Adv. Mater.* **2011**, *23*, 147-179.
7. Wilson, D. L.; Martin, R.; Hong, S.; Cronin-Golomb, M.; Mirkin, C. A.; Kaplan, D. L. Surface Organization and Nanopatterning of Collagen by Dip-Pen Nanolithography. *Proc. Natl. Acad. Sci. U. S. A.* **2001**, *98*, 13660-13664.
8. El Garah, M.; Marets, N.; Mauro, M.; Aliprandi, A.; Bonacchi, S.; De Cola, L.; Ciesielski, A.; Bulach, V.; Hosseini, M. W.; Samori, P. Nanopatterning of Surfaces with Monometallic and

Heterobimetallic 1D Coordination Polymers: A Molecular Tectonics Approach at the Solid/Liquid Interface. *J. Am. Chem. Soc.* **2015**, *137*, 8450-8459.

9. Barrios, C. A.; Canalejas-Tejero, V. A Top-Down Approach for Fabricating Three-Dimensional Closed Hollow Nanostructures with Permeable Thin Metal Walls. *Beilstein J. Nanotechnol.* **2017**, *8*, 1231-1237.
10. Oleske, K. W.; Barteau, K. P.; Beaucage, P. A.; Asenath-Smith, E.; Wiesner, U.; Estroff, L. A. Nanopatterning of Crystalline Transition Metal Oxides by Surface Templated Nucleation on Block Copolymer Mesostructures. *Cryst. Growth Des.* **2017**, *17*, 5775-5782.
11. Goronzy, D. P.; Ebrahimi, M.; Rosei, F.; Arramel; Fang, Y.; De Feyter, S.; Tait, S. L.; Wang, C.; Beton, P. H.; Wee, A. T. S.; Weiss, P. S.; Perepichka, D. F. Supramolecular Assemblies on Surfaces: Nanopatterning, Functionality, and Reactivity. *ACS Nano* **2018**, *12*, 7445-7481.
12. Phan, T. H.; Wandelt, K. Redox-Activity and Self-Organization of Iron-Porphyrin Monolayers at a Copper/Electrolyte Interface. *J. Chem. Phys.* **2015**, *142*, 101917.
13. Madueno, R.; Räisänen, M. T.; Silien, C.; Buck, M. Functionalizing Hydrogen-Bonded Surface Networks with Self-Assembled Monolayers. *Nature* **2008**, *454*, 618.
14. Mali, K. S.; Pearce, N.; De Feyter, S.; Champness, N. R. Frontiers of Supramolecular Chemistry at Solid Surfaces. *Chem. Soc. Rev.* **2017**, *46*, 2520-2542.
15. Cao, H.; Waghay, D.; Knoppe, S.; Dehaen, W.; Verbiest, T.; De Feyter, S. Tailoring Atomic Layer Growth at the Liquid-Metal Interface. *Nat. Commun.* **2018**, *9*, 4889.
16. Wick, P.; Louw-Gaume, A. E.; Kucki, M.; Krug, H. F.; Kostarelos, K.; Fadeel, B.; Dawson, K. A.; Salvati, A.; Vázquez, E.; Ballerini, L.; Tretiach, M.; Benfenati, F.; Flahaut, E.; Gauthier, L.; Prato, M.; Bianco, A. Classification Framework for Graphene-Based Materials. *Angew. Chem., Int. Ed.* **2014**, *53*, 7714-7718.
17. Yu, X.; Cheng, H.; Zhang, M.; Zhao, Y.; Qu, L.; Shi, G. Graphene-Based Smart Materials. *Nat. Rev. Mater.* **2017**, *2*, 17046.
18. Fu, K.; Yao, Y.; Dai, J.; Hu, L. Progress in 3D Printing of Carbon Materials for Energy-Related Applications. *Adv. Mater.* **2017**, *29*, 1603486.
19. Georgakilas, V.; Otyepka, M.; Bourlinos, A. B.; Chandra, V.; Kim, N.; Kemp, K. C.; Hobza, P.; Zboril, R.; Kim, K. S. Functionalization of Graphene: Covalent and Non-Covalent Approaches, Derivatives and Applications. *Chem. Rev.* **2012**, *112*, 6156-6214.
20. Mali, K. S.; Greenwood, J.; Adisoejoso, J.; Phillipson, R.; De Feyter, S. Nanostructuring Graphene for Controlled and Reproducible Functionalization. *Nanoscale* **2015**, *7*, 1566-1585.
21. Velpula, G.; Teyssandier, J.; De Feyter, S.; Mali, K. S. Nanoscale Control over the Mixing Behavior of Surface-Confined Bicomponent Supramolecular Networks Using an Oriented External Electric Field. *ACS Nano* **2017**, *11*, 10903-10913.
22. MacLeod, J. M.; Rosei, F. Molecular Self-Assembly on Graphene. *Small* **2014**, *10*, 1038-1049.
23. Järvinen, P.; Hämäläinen, S. K.; Banerjee, K.; Häkkinen, P.; Ijäs, M.; Harju, A.; Liljeroth, P. Molecular Self-Assembly on Graphene on SiO<sub>2</sub> and h-BN Substrates. *Nano Lett.* **2013**, *13*, 3199-3204.

24. Greenwood, J.; Phan, T. H.; Fujita, Y.; Li, Z.; Ivasenko, O.; Vanderlinden, W.; Van Gorp, H.; Frederickx, W.; Lu, G.; Tahara, K.; Tobe, Y.; Uji-i, H.; Mertens, S. F. L.; De Feyter, S. Covalent Modification of Graphene and Graphite Using Diazonium Chemistry: Tunable Grafting and Nanomanipulation. *ACS Nano* **2015**, *9*, 5520-5535.
25. Criado, A.; Melchionna, M.; Marchesan, S.; Prato, M. The Covalent Functionalization of Graphene on Substrates. *Angew. Chem., Int. Ed.* **2015**, *54*, 10734-10750.
26. Englert, J. M.; Dotzer, C.; Yang, G.; Schmid, M.; Papp, C.; Gottfried, J. M.; Steinrück, H.-P.; Spiecker, E.; Hauke, F.; Hirsch, A. Covalent Bulk Functionalization of Graphene. *Nat. Chem.* **2011**, *3*, 279.
27. He, Y.; Garnica, M.; Bischoff, F.; Ducke, J.; Bocquet, M.-L.; Batzill, M.; Auwärter, W.; Barth, J. V. Fusing Tetrapyrroles to Graphene Edges by Surface-Assisted Covalent Coupling. *Nat. Chem.* **2016**, *9*, 33.
28. Faghani, A.; Donskyi, I. S.; Fardin Gholami, M.; Ziem, B.; Lippitz, A.; Unger, W. E. S.; Böttcher, C.; Rabe, J. P.; Haag, R.; Adeli, M. Controlled Covalent Functionalization of Thermally Reduced Graphene Oxide to Generate Defined Bifunctional 2D Nanomaterials. *Angew. Chem., Int. Ed.* **2017**, *56*, 2675-2679.
29. Huynh, T. M. T.; Phan, T. H.; Ivasenko, O.; Mertens, S. F. L.; De Feyter, S. Nanoconfined Self-Assembly on a Grafted Graphitic Surface under Electrochemical Control. *Nanoscale* **2017**, *9*, 362-368.
30. Cui, K.; Mali, K. S.; Wu, D.; Feng, X.; Müllen, K.; Walter, M.; De Feyter, S.; Mertens, S. F. L. Reversible Anion-Driven Switching of an Organic 2D Crystal at a Solid-Liquid Interface. *Small* **2017**, *13*, 1702379.
31. Hossain, M. Z.; Walsh, M. A.; Hersam, M. C. Scanning Tunneling Microscopy, Spectroscopy, and Nanolithography of Epitaxial Graphene Chemically Modified with Aryl Moieties. *J. Am. Chem. Soc.* **2010**, *132*, 15399-15403.
32. Van Gorp, H.; Walke, P.; Bragança, A. M.; Greenwood, J.; Ivasenko, O.; Hirsch, B. E.; De Feyter, S. Self-Assembled Polystyrene Beads for Templated Covalent Functionalization of Graphitic Substrates Using Diazonium Chemistry. *ACS Appl. Mater. Interfaces* **2018**, *10*, 12005-12012.
33. Gross, A. J.; Nock, V.; Polson, M. I. J.; Alkaiji, M. M.; Downard, A. J. Surface Patterning Using Two-Phase Laminar Flow and *in situ* Formation of Aryldiazonium Salts. *Angew. Chem., Int. Ed.* **2013**, *52*, 10261-10264.
34. Anariba, F.; DuVall, S. H.; McCreery, R. L. Mono- and Multilayer Formation by Diazonium Reduction on Carbon Surfaces Monitored with Atomic Force Microscopy "Scratching". *Anal. Chem.* **2003**, *75*, 3837-3844.
35. Brooksby, P. A.; Downard, A. J. Nanoscale Patterning of Flat Carbon Surfaces by Scanning Probe Lithography and Electrochemistry. *Langmuir* **2005**, *21*, 1672-1675.
36. Verstraete, L.; Greenwood, J.; Hirsch, B. E.; De Feyter, S. Self-Assembly under Confinement: Nanocorrals for Understanding Fundamentals of 2D Crystallization. *ACS Nano* **2016**, *10*, 10706-10715.

37. Seibel, J.; Verstraete, L.; Hirsch, B. E.; Bragança, A. M.; De Feyter, S. Biasing Enantiomorph Formation *via* Geometric Confinement: Nanocorrals for Chiral Induction at the Liquid–Solid Interface. *J. Am. Chem. Soc.* **2018**, *140*, 11565-11568.
38. Corgier, B. P.; Bélanger, D. Electrochemical Surface Nanopatterning Using Microspheres and Aryldiazonium. *Langmuir* **2010**, *26*, 5991-5997.
39. Xia, Z.; Leonardi, F.; Gobbi, M.; Liu, Y.; Bellani, V.; Liscio, A.; Kovtun, A.; Li, R.; Feng, X.; Orgiu, E.; Samorì, P.; Treossi, E.; Palermo, V. Electrochemical Functionalization of Graphene at the Nanoscale with Self-Assembling Diazonium Salts. *ACS Nano* **2016**, *10*, 7125-7134.
40. Tahara, K.; Ishikawa, T.; Hirsch, B. E.; Kubo, Y.; Brown, A.; Eyley, S.; Daukiya, L.; Thielemans, W.; Li, Z.; Walke, P.; Hirose, S.; Hashimoto, S.; De Feyter, S.; Tobe, Y. Self-Assembled Monolayers as Templates for Linearly Nanopatterned Covalent Chemical Functionalization of Graphite and Graphene Surfaces. *ACS Nano* **2018**, *12*, 11520-11528.
41. Delamar, M.; Hitmi, R.; Pinson, J.; Saveant, J. M. Covalent Modification of Carbon Surfaces by Grafting of Functionalized Aryl Radicals Produced from Electrochemical Reduction of Diazonium Salts. *J. Am. Chem. Soc.* **1992**, *114*, 5883-5884.
42. Baranton, S.; Bélanger, D. Electrochemical Derivatization of Carbon Surface by Reduction of in Situ Generated Diazonium Cations. *J. Phys. Chem. B* **2005**, *109*, 24401-24410.
43. Richard, W.; Evrard, D.; Gros, P. New insight into 4-nitrobenzene diazonium reduction process: Evidence for a grafting step distinct from NO<sub>2</sub> electrochemical reactivity. *J. Electroanal. Chem.* **2012**, *685*, 109–115.
44. Ferrari, A. C.; Basko, D. M. Raman Spectroscopy as a Versatile Tool for Studying the Properties of Graphene. *Nat. Nanotechnol.* **2013**, *8*, 235-246.
45. Sequeira, C. A. C.; Santos, D. M. F.; Šljukić, B.; Amaral, L. Physics of Electrolytic Gas Evolution. *Braz. J. Phys.* **2013**, *43*, 199–208.
46. Juergens, N. The Biological Underpinnings of Namib Desert Fairy Circles. *Science* **2013**, *339*, 1618-1621.
47. Zhang, X.; Winnik, F. M. Preface to the Nanobubbles Special Issue. *Langmuir* **2016**, *32*, 11071-11071.
48. Li, M.; Tonggu, L.; Zhan, X.; Mega, T. L.; Wang, L. Cryo-EM Visualization of Nanobubbles in Aqueous Solutions. *Langmuir* **2016**, *32*, 11111-11115.
49. Galli, C. Radical Reactions of Arenediazonium Ions: An Easy Entry into the Chemistry of the Aryl Radical. *Chem. Rev.* **1988**, *88*, 765-792.
50. Cui, L.; Xu, Y.; Liu, B.; Yang, W.; Song, Z.; Liu, J. Well-Controlled Preparation of Evenly Distributed Nanoporous HOPG Surface *via* Diazonium Salt Assisted Electrochemical Etching Process. *Carbon* **2016**, *102*, 419-425.
51. Mertens, S. F. L.; Hemmi, A.; Muff, S.; Gröning, O.; De Feyter, S.; Osterwalder, J.; Greber, T. Switching stiction and adhesion of a liquid on a solid. *Nature* **2016**, *534*, 676–679.
52. Gadallah, F. F.; Elofson, R. M. Arylation of Aromatic Compounds by Electrochemical Reduction of Benzenediazonium Tetrafluoroborate in Aprotic Solvents. *J. Org. Chem.* **1969**, *34*, 3335-3338.

53. Combellas, C.; Jiang, D.-E.; Kanoufi, F.; Pinson, J.; Podvorica, F. I. Steric Effects in the Reaction of Aryl Radicals on Surfaces. *Langmuir* **2009**, *25*, 286-293.
54. Verstraete, L.; Hirsch, B. E.; Greenwood, J.; De Feyter, S. Confined Polydiacetylene Polymerization Reactions for Programmed Length Control. *Chem. Commun.* **2017**, *53*, 4207-4210.
55. Deshpande, A.; Sham, C.-H.; Alaboson, J. M. P.; Mullin, J. M.; Schatz, G. C.; Hersam, M. C. Self-Assembly and Photopolymerization of Sub-2 nm One-Dimensional Organic Nanostructures on Graphene. *J. Am. Chem. Soc.* **2012**, *134*, 16759-16764.
56. Giridharagopal, R.; Kelly, K. F. Substrate-Dependent Properties of Polydiacetylene Nanowires on Graphite and MoS<sub>2</sub>. *ACS Nano* **2008**, *2*, 1571-1580.
57. Guo, C.; Xue, J. D.; Cheng, L. X.; Liu, R. C.; Kang, S. Z.; Zeng, Q. D.; Li, M. Two-Dimensional Self-Assembly of Diacetylenic Acid Derivatives and Their Light-Induced Polymerization on HOPG Surfaces. *Phys. Chem. Chem. Phys.* **2017**, *19*, 16213-16218.
58. Bang, J. J.; Rupp, K. K.; Russell, S. R.; Choong, S. W.; Claridge, S. A. Sitting Phases of Polymerizable Amphiphiles for Controlled Functionalization of Layered Materials. *J. Am. Chem. Soc.* **2016**, *138*, 4448-4457.
59. Sullivan, S. P.; Schnieders, A.; Mbugua, S. K.; Beebe, T. P. Controlled Polymerization of Substituted Diacetylene Self-Organized Monolayers Confined in Molecule Corrals. *Langmuir* **2005**, *21*, 1322-1327.
60. Wilms, M.; Kruff, M.; Bermes, G.; Wandelt, K. A New and Sophisticated Electrochemical Scanning Tunneling Microscope Design for the Investigation of Potentiodynamic Processes. *Rev. Sci. Instrum.* **1999**, *70*, 3641-3650.

ToC graphic:

### Covalent nanostructured patterning

